Optical coherence tomography imaging and noise characterization based on 1-μm microresonator frequency combs

Cite as: APL Photon. 9, 086105 (2024); doi: 10.1063/5.0215574
Submitted: 24 April 2024 • Accepted: 1 August 2024 •
Published Online: 15 August 2024

T. Melton,[1,a)] J. F. McMillan,[1] J. Yang,[1] W. Wang,[1] Y. Lai,[2] M. Gerber,[2] M. Rodriguez,[2] J. P. Hubschman,[2] K. Nouri-Mahdavi,[2,a)] and C. W. Wong[1,a)]

AFFILIATIONS

[1] Mesoscopic Optics and Quantum Electronics Laboratory, University of California, Los Angeles, California 90095, USA
[2] Stein Eye Institute, David Geffen School of Medicine at University of California, Los Angeles, California 90095, USA

[a)] **Authors to whom correspondence should be addressed:** tristanmelton@engineering.ucla.edu; nouri-mahdavi@jsei.ucla.edu; and cheewei.wong@ucla.edu

ABSTRACT

Spectral-domain optical coherence tomography is a pervasive, non-invasive, *in vivo* biomedical imaging platform that currently utilizes incoherent broadband superluminescent diodes to generate interferograms from which depth and structural information are extracted. Advancements in laser frequency microcombs have enabled the chip-scale broadband generation of discrete frequency sources, with prior soliton and chaotic comb states examined in discrete spectral-domain optical coherence tomography at 1.3 μm. In this work, we demonstrate coherence tomography through Si_3N_4 microresonator laser frequency microcombs at 1 μm, achieving imaging qualities on-par with or exceeding the equivalent commercial optical coherence tomography system. We characterize the noise performance of our frequency comb states and additionally show that inherent comb line amplitude fluctuations in a chaotic state and the resultant tomograms can be compensated via multi-scan averaging.

I. INTRODUCTION

Optical coherence tomography (OCT), developed by Huang *et al.* in 1991,[1] has become a crucial pervasive technique for non-invasive imaging of biological tissue *in vivo*, with applications in ophthalmology,[2–4] intravascular imaging,[5] and brain imaging.[6–8] Improvements in frequency domain OCT (FD-OCT) methodology, such as the advent of spectral-domain OCT (SD-OCT) and swept-source OCT (SS-OCT), have led to much higher sensitivities and acquisition speeds, exceeding those of time domain OCT (TD-OCT).[9–13] Uniquely, the implementation of discrete frequency light sources to replace the standard continuous spectrum superluminescent diodes and supercontinuum-generation sources[14] for imaging has been theoretically and experimentally demonstrated to improve depth sensitivity, dramatically reducing the rate of sensitivity falloff above 0.5 mm compared to conventional continuous light sources, which experience a 19 dB sensitivity falloff from 0.5 to ≈3.5 mm.[15] In addition, discrete frequency sources allow reduced interpixel crosstalk[15,16] and lower tissue power exposure, with little to no impact on the resulting tomogram axial resolution.[17] Periodicity added to the tomogram inherent with this technique allows optical domain subsampling to significantly extend the OCT imaging range.[18] One promising discrete frequency light source is the laser frequency microcomb, specifically generated via high quality factor nonlinear microresonator structures through the optical Kerr effect and other nonlinear processes within a resonant structure.[19–24] These chip-scale combs are driven by a continuous-wave laser source, with the comb free spectral range determined predominantly by the microresonator radius.[25–28] Implemented in CMOS-compatible photonic foundry lines, these laser frequency microcombs allow significant miniaturization and cost reduction with high yields and tight process control through the semiconduc-

tor technology ecosystem and instrumentation. With precise dispersion engineering of the microresonator waveguide, the microcombs' spectral bandwidth can reach and even exceed an octave, allowing for carrier envelope phase and optical frequency stabilization through f–$2f$ interferometry.[29,30] Further improvements in nanofabrication technology have allowed for even longer cavity lifetimes and higher Q factors, drastically reducing the power threshold for microcomb generation.[31,32] These microcombs have been generated, for example, on multiple chip-scale platforms such as silica,[19,33,34] silicon nitride,[27,35–50] aluminum nitride,[51] crystalline fluorides,[52,53] diamonds,[54] and AlGaAs.[55]

In this work, we demonstrate, for the first time to the authors' knowledge, laser frequency microcomb-based 1 μm OCT imaging with 5.65 ± 1.7 μm axial resolution exceeding the instrument-measured 20 μm resolution of the same commercial Telesto II optical coherence tomography system utilized. We characterize the free spectral range (FSR), bandwidth, and relative intensity noise (RIN) of several different microcombs to ascertain their viability as discrete OCT light sources. A custom spectrometer is utilized to surpass the instrument-limited axial resolution. We image several example samples and examine the multi-scan averaging scaling between our frequency microcombs and superluminescent diodes

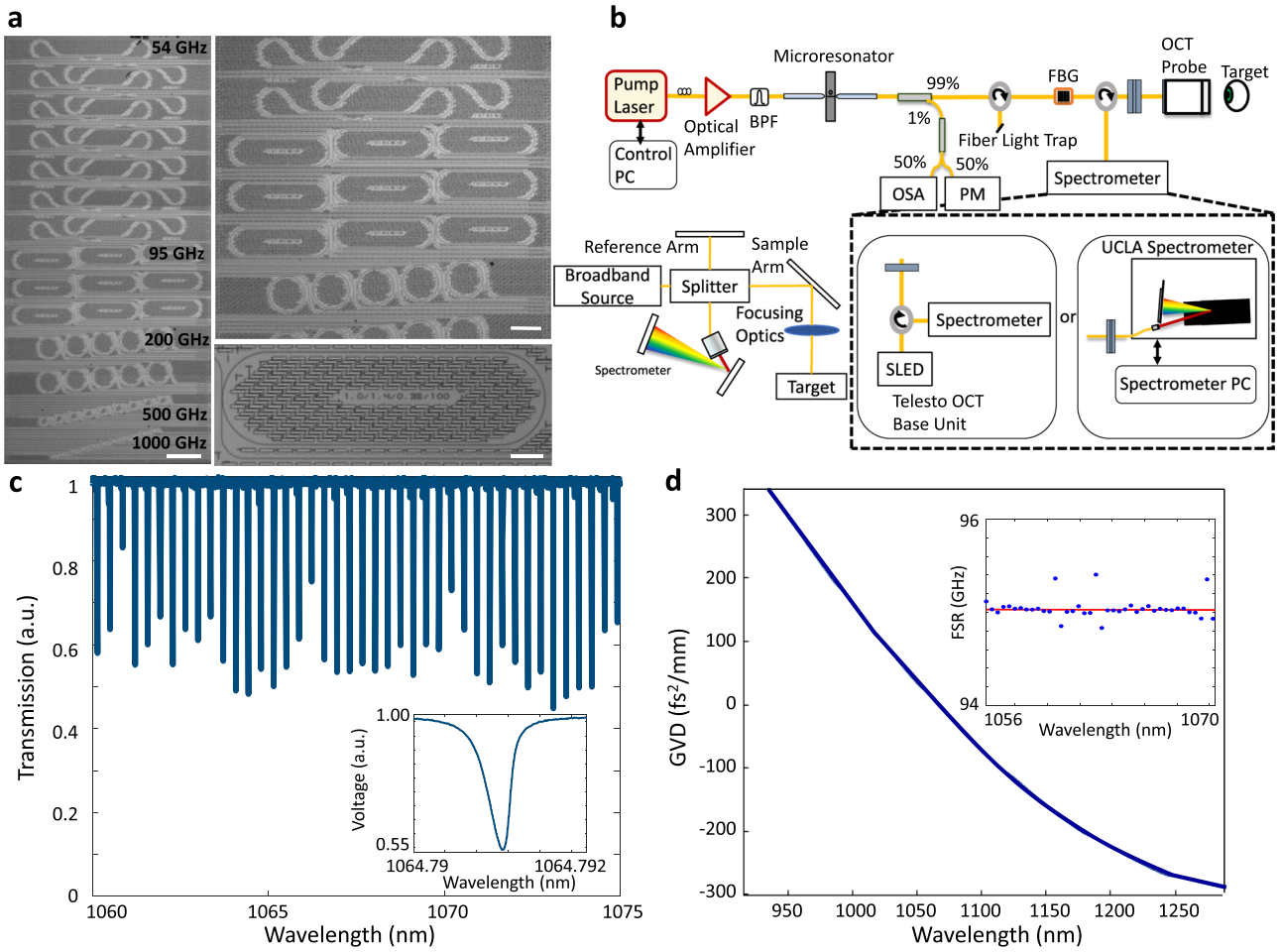

FIG. 1. Characteristics of the laser frequency microcomb resonator for optical coherence tomography imaging. (a) Microresonator laser frequency microcomb chips nanofabricated at LiGenTec with FSRs varying from 50 GHz to 1 THz. The resonator shown in the bottom right is used for 95 GHz OCT imaging. Scale bars from left and clockwise: 500, 250, 100 μm. (b) Overview of SD-OCT and system diagram. A pump laser (Sacher Lasertechnik P-1060-0420-01112) is amplified by an ytterbium-doped fiber amplifier (YDFA) and coupled into the SiN microresonator chip via lensed fibers. 1% of the output is tapped into an optical spectrum analyzer (OSA) and a power meter (PM), while the remaining 99% passes through a grating to filter out the pump so as not to saturate the downstream optical components and spectrometer. After passing through a circulator, the comb state enters the OCT probe optics and interacts with the imaging target. Reflected light passes back through the circulator to either the internal Telesto II spectrometer or the custom-built UCLA spectrometer (see the supplementary material). A schematic of the general operating principle of SD-OCT is presented in the bottom left subpanel, where a broadband source is sent through a Michaelson interferometer, with one arm containing relevant optics and the imaging target. The interference pattern is diffracted onto a spectrometer, and the interferogram is recorded. (c) Swept-wavelength interferometry (SWI) of the aforementioned microresonator resonances. Inset: Zoomed-in of a single resonance. (d) Simulated GVD vs wavelength. Inset: Measured GVD at −39.9 fs2/mm utilizing the aforementioned SWI metrology.

(SLDs). We further provide quantitative analysis of our laser microcomb tomograms through indices of maximum tissue contrast index (mTCI)[56] in conjunction with intensity ratio (IR), tissue signal ratio (TSR), and quality index (QI)[57] to verify the advantages of our discrete frequency SD-OCT system over SLD-based commercial OCT systems.

II. MICRORESONATOR AND FREQUENCY MICROCOMB GENERATION

We designed the 1-μm-wavelength microresonators on the low-pressure chemical vapor deposition stoichiometric silicon nitride platform. Our frequency microcomb resonators, as shown in Fig. 1(a), have free-spectral ranges (FSRs) of 54, 95, 200, 500 GHz, and 1 THz, with anomalous group velocity dispersion (GVD) engineered via the waveguide cross-sectional area. Microresonator GVD is simulated and optimized in COMSOL via an axisymmetric finite element method to reduce simulation time with ring width variation to fine-tune the dispersion parameter. The simulated refractive index data are then exported to MATLAB to calculate the dispersion parameter and for further analysis. Once the desired dispersion has been achieved, the device is simulated in Lumerical using the frequency-difference time domain method to optimize the coupling between the bus and ring at the desired pump frequency, using the bus-to-ring gap as the optimizing variable. Once a suitable ring gap is found, chiplets are created for fabrication using Python with variations in ring width and coupling gap to account for fabrication errors by the foundry. The microcombs are fabricated at LiGenTec. The microcombs, initiated by nonlinear frequency conversion via non-degenerate four-wave mixing and self- and cross-phase modulation within the cavity,[19] enable optical gain at nearby optical modes to the pumped resonant mode and cascade to form a variety of microcomb states, from modulation instability to chaotic combs,[22,23,25,26,35–39,41,45] breather combs,[41,58] and soliton states.[25,38,45,59] Comb generation is initiated by sweeping the pump laser frequency from the effective blue- to red-detuned side of the pumped cavity resonance until the desired comb state is generated.

The experimental setup for microcomb generation is illustrated in the top panel of Fig. 1(b). Utilizing swept wavelength interferometry,[22] the 95 GHz resonator is characterized as having anomalous GVD, as shown in Figs. 1(c) and 1(d). To optimize the OCT measurements, the comb states are specifically chosen to tune the desired imaging parameters. For optimal tomograms, the comb lines should have approximately the same intensities so as to produce the widest possible spectral bandwidth and to reduce the need for post-processing involving comb line normalization.[18] In addition, any set of comb lines that have a significantly higher intensity than the surrounding lines can add non-uniformity and noise in the form of markedly brighter pixels and risk saturating the spectrometer, degrading the resulting OCT image. Avoided mode crossings can also result in tomogram degradation in a similar manner since these comb line pixel intensities are reduced relative to other brightly reflecting pixels, effectively cutting them out of the resulting tomogram. Optimization of these qualitative parameters is broadly applicable to the frequency comb states, with the comb bandwidth and microresonator free spectral range being key quantitative parameters for discrete frequency OCT, controlling,

TABLE I. Selected frequency comb FSR and corresponding theoretical maximum imaging depth in the tissue and the air. The bold row is from this work.

Frequency comb free spectral range (GHz)	Imaging depth	
	In air (mm)	In tissue (n = 1.4) (mm)
1000	0.075	0.05
200	0.37	0.27
95	**0.94**	**0.67**
54	1.4	1.0
27	2.7	1.9

TABLE II. Selected frequency comb spectral bandwidth and corresponding theoretical axial resolution estimate. The bold row is from this work.

Spectral bandwidth full width half maximum (nm)	Axial resolution central central wavelength = 1064 nm	
	In air (μm)	In tissue (n = 1.4) (μm)
30	27	12
80	**6.2**	**4.5**
100	5.0	3.5
200	2.5	1.8
300	1.6	1.1

respectively, the axial resolution and imaging depth. For example, the axial resolution is determined via

$$z = \frac{2\ln(2)\lambda_c^2}{\pi\Delta\lambda_{BW}}, \tag{1}$$

where λ_c is the light source center wavelength and $\Delta\lambda_{BW}$ represents the frequency microcomb light source bandwidth.[60]

The microcomb bandwidth is determined predominantly by the (small) anomalous GVD magnitude of the resonator at the pump wavelength. The maximum imaging depth is likewise obtained via

$$z_{\max} = \frac{\lambda_c^2}{4\delta_s}, \tag{2}$$

where δ_s is the spectrometer sampling interval. When the spectrometer sampling interval is perfectly matched to the comb line spacing, the imaging depth increases as the FSR decreases. From both expressions, we see that a general trade-off between imaging depth and axial resolution arises—as FSR decreases (larger imaging depth), the spectral bandwidth of the resultant comb typically decreases, which leads to poorer axial resolution. As a result, the maximum imaging depth and axial resolution have an inverse relationship, as illustrated in Tables I and II.

In addition, the coupling between different transverse mode families in the multimode waveguide resonator results in avoided mode crossings, adding a periodic amplitude modulation that occurs more frequently as the FSR decreases.[22,61] Figure 2 shows the generated laser microcomb states and their corresponding measured relative intensity noise (RIN). For the 54 GHz microresonator comb, several aberrations from avoided-mode crossings are present in

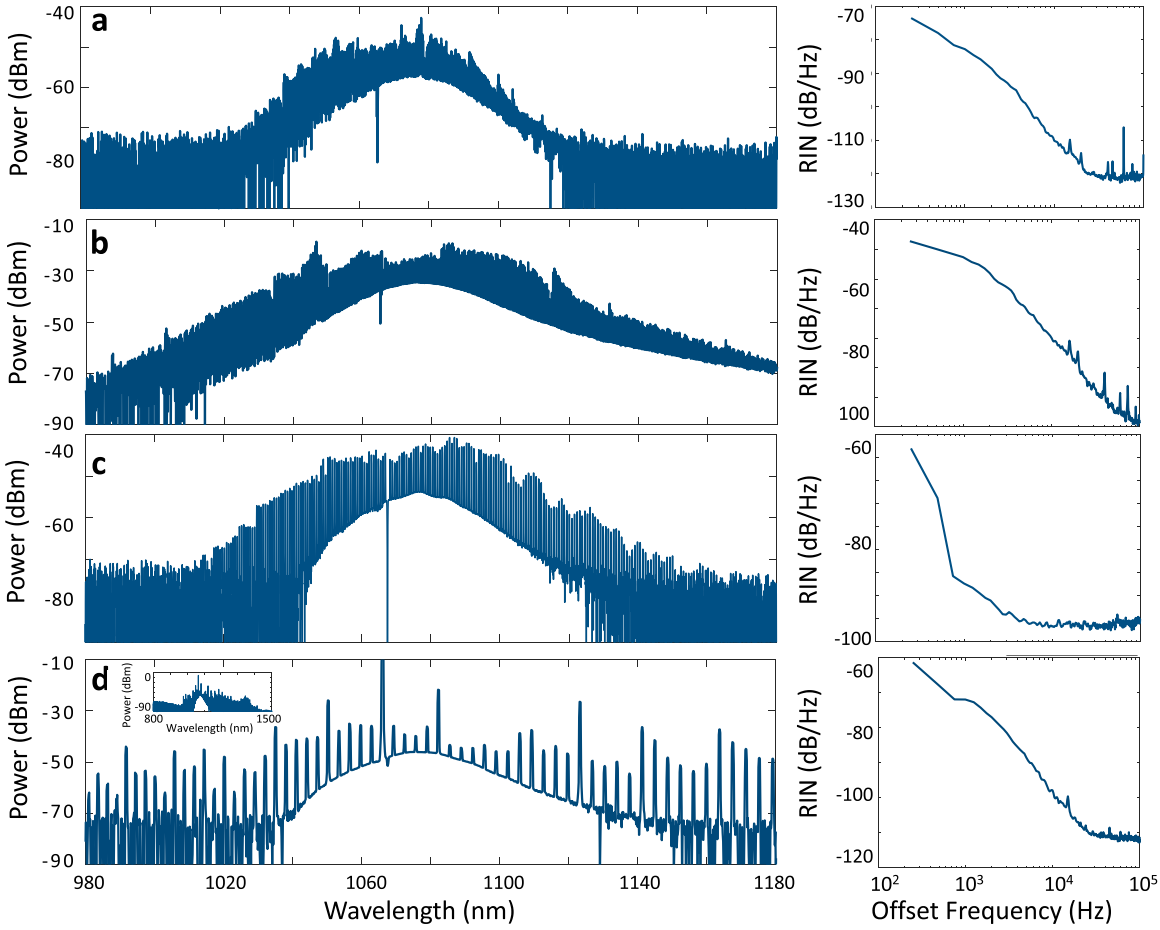

FIG. 2. Selected chaotic comb spectra with multiple FSRs. (a)–(d), 54, 95, 200 GHz, and 1 THz comb spectra, respectively, with corresponding relative intensity noise (RIN) measurements on the right column. An ideal comb state should have a smooth envelope with a broad spectrum while maintaining a small free spectral range for increased imaging depth. A high RIN denotes significant intensity fluctuations, which adversely affect the image clarity of a single tomogram.

Fig. 2(a), which can deteriorate the resulting tomogram, and its relatively narrow bandwidth can limit the axial resolution. The 200 GHz microresonator comb in Fig. 2(c) is smoother with a broader bandwidth and provides high axial resolution; however, the high FSR reduces the imaging depth to values that are relatively low for effective clinical usage in an OCT system. The 1 THz microcomb spectrum in Fig. 2(d) has similar attributes, with a broader comb bandwidth, but the larger FSR reduces the imaging depth outside of practical OCT applications other than very thin tissue samples.

In contrast, the 95 GHz microcomb spectrum—as illustrated in Fig. 2(b)—only has a few avoided-mode crossings, and its balanced FSR and comb spectral bandwidth of ~80 nm allow for an acceptable trade-off for the in-tissue imaging depth at 500 μm and a theoretical axial resolution in the air of 6.2 μm. Based on these factors and the accessible comb states, we chose the laser microcomb with 95 GHz FSR to optimize tomogram clarity and resolution without sacrificing much imaging depth. In comparison, the commercial SLD has a center wavelength of 1064 nm with a 3 dB bandwidth of 90 nm. We also have the option of choosing between a chaotic comb state and a dispersive Kerr soliton. While the chaotic state allows for a wider flat peak due to the more available nonlinear dynamical routes for a chaotic microcomb formation,[38] additional comb line amplitude noise is introduced, which might lead to a smaller signal-to-noise ratio (SNR) in the tomogram.[18,60]

Conversely, the dispersive Kerr soliton has an envelope following a hyperbolic secant squared profile and has a smaller 3 dB optical bandwidth compared to the chaotic comb state. The soliton state has fewer individual comb line amplitude fluctuations due to the inherent phase- and mode-locking.[22,62] A chaotic comb state is still preferred since by taking multiple scans, the effects of individual comb line fluctuations can be nearly eliminated by averaging tomograms together (Sec. IV below), overcoming the primary drawback of the chaotic comb state. In this work, we average ten scans per completed tomogram.

III. SOFTWARE PROCESSING

To ascertain the OCT system's axial resolution, we take the tomogram of a reflector and fit the resulting Gaussian peak as shown in Fig. 3(a). With the full-width half-maximum of the resulting fit, we calculate the system axial resolution utilizing the specific comb state. To obtain this measurement, we utilize a beam splitter as our reflector and find an effective axial resolution of 5.65 ± 1.7 μm, which well matches the theoretical in-air estimate of 6.2 μm, shown earlier in Table II. We term this the effective axial resolution since the fitting is performed post-processing.

The software processing flow for microcomb OCT imaging is shown in Fig. 3(b). Prior to post-processing, a calibration is performed to correct the nonlinear mapping of the spectrometer grating as well as the wavevector phase variation from residual dispersion in the reference and target arms.[63] We define the detected spectrum for a single reflector with reflectivity r_s as

$$I_{\mathrm{det}}(k) = \frac{1}{4} I_{source}(k)\left(1 + r_s + 2\sqrt{r_s}\,\cos\left(2k\Delta z + \Phi_d(k)\right)\right). \quad (3)$$

After taking two measurements of the simple reflector slightly separated from one another, the phase component can be extracted using the Hilbert transform, which, therefore, determines the wavenumber correction vector and residual dispersion using

$$\phi_1(n) = 2k(z_1 - z_s) + \phi_d, \quad (4)$$

$$\phi_2(n) = 2k(z_2 - z_s) + \phi_d, \quad (5)$$

$$\Delta\phi(n) = \phi_1(n) - \phi_2(n), \quad (6)$$

where k is the wavevector; z_1, z_2, and z_s are the first, second, and starting distances, respectively; and ϕ_d is the correction. This correction can then be applied in the processing stack to improve tomogram clarity. Subsequently, several processing steps are applied to cleanly extract the tomograms from the interferograms measured by our frequency microcomb OCT subsystem and improve their quality. First, we perform a background noise subtraction and then apply a Gaussian filter in the form of a moving average window to the interferogram to spectrally shape the data to match a Gaussian function more closely and reduce noise.[64,65] A window width that is too wide or narrow washes out any internal structure and leaves only the strong reflecting surfaces visible. It must be manually tuned to find the appropriate width, as shown in Figs. 3(c1)–3(c3). Next, apodization is applied to the spectrum in the form of a Hann window to preserve the bandwidth of the interferogram and drive down the noise floor.

Furthermore, as shown in Figs. 3(d1) and 3(e), the utilization of a Blackman window instead of a Hann window has little qualitative effect on the resulting tomogram, indicating our bandwidth is well-preserved and not apodization limited. Furthermore, in processing the tomograms, we note that the phase corrections calculated during the calibration step are applied via a spline interpolation. The fast Fourier transform is applied to the final set of interferograms to obtain the final tomogram.[63–65] Figures 3(d1) and 3(d2) illustrate the effect of averaging the 95 GHz chaotic microcomb B-scan over ten tomograms. The same configuration and target position are kept

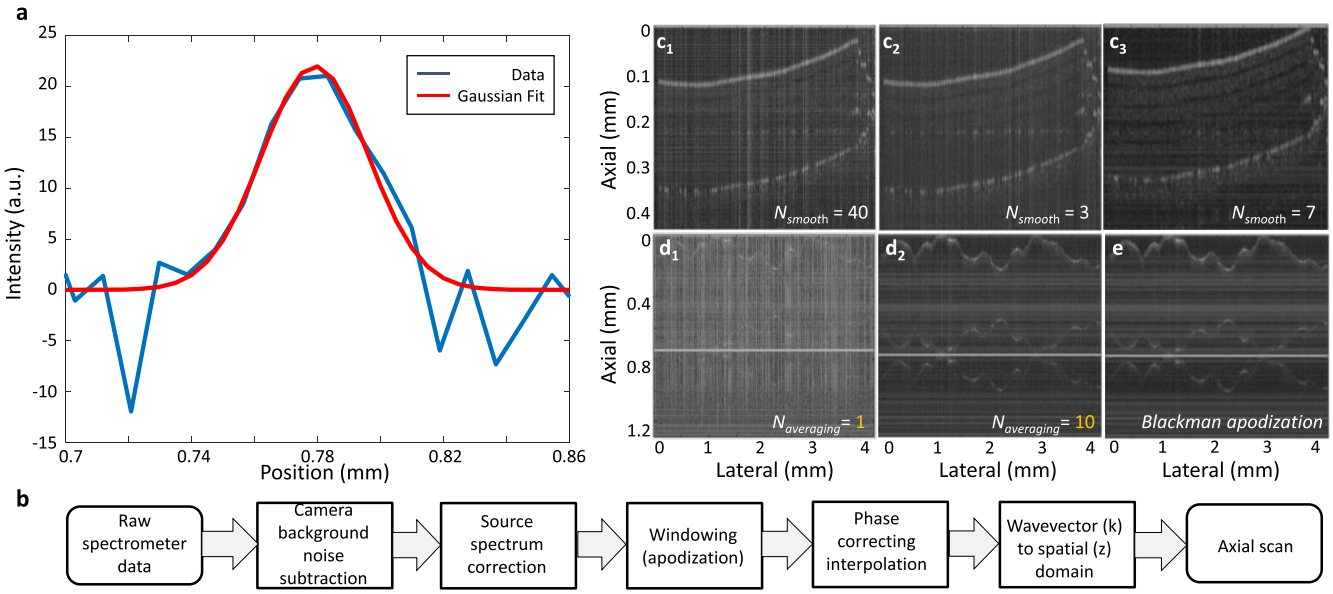

ure 4 Volumetric frequency microcomb OCT imaging post processing source spectrum correction and multi scan

FIG. 3. Volumetric frequency microcomb OCT imaging, post-processing, source spectrum correction, and multi-scan averaging. (a) Measurement of the axial resolution of the system, with Gaussian fitting in red. The full-width half-maximum of the Gaussian fit illustrates an axial resolution of 5.65 ± 1.7 μm. (b) Post-processing steps for optimal OCT image results. (c_1)–(c_3) Effect of source spectrum correction via a Gaussian moving window with widths of 40, 3, and 7 applied to a tape stack tomogram. (d_1)–(d_2) Effect of multi-scan averaging to reduce the chaotic comb A-scan noise and improve SNR applied to orange peel tomogram. (e) Ten-averaged OCT image utilizing Blackman apodization for bandwidth improvement instead of the Hann window.

for each B-scan. We observe that the effect of spurious saturated A-scans is reduced, which previously appeared as vertical artifacts from a chaotic microcomb source, improving the final output imaging tomogram.

IV. OCT IMAGES AND IMAGE QUALITY QUANTIFICATION

With the generated microcombs, we obtain frequency microcomb OCT images of three example subsystems: a tape stack, an orange peel, and a pig retina, to test the OCT imaging capabilities. This is illustrated in Fig. 4. All samples in this work have an A-scan rate of 76-kHz and utilize Blackman apodization. All frequency comb OCT tomograms are the result of ten averaged scans, except for the volumetric scan, which is a single scan. B-scans are acquired in sets and passed through a series of post-processing steps,[63] with the resulting tomograms averaged to increase the SNR. First, we image a six-layer stack of painter Scotch tape using the built-in Telesto-II SLD as a reference and a 95 GHz frequency comb for direct comparison, utilizing a custom-built spectrometer (see the supplementary material). We hold all other experimental variables constant except for the Fourier transform post-processing of the frequency comb-driven tomogram. Qualitatively, both the frequency comb tomogram [Fig. 4(a)] and the SLD tomogram [Fig. 4(b)] can be observed to be nearly identical, with all features of the tape stack present in both. The edges between each tape layer are clear and distinct, and the layer of painter's tape on the bottom of the stack can also be observed. The inset in each figure represents the post-processed interferograms used to create the images. The interferogram for the SLD-lit source has a smooth Gaussian-envelope over multiple B-scans, which naturally lends itself to a clean Fourier transform to view the image. The interferogram for the frequency comb after post-processing is also fairly Gaussian but has spurious frequencies and also contains noticeable gaps, a result of the avoided mode crossings within the comb state and a fiber Bragg grating to remove the pump to avoid saturation of the spectrometer. Fortunately, because the overall interferogram is still roughly Gaussian and multiple scans are averaged together, the tomogram results are still clear and qualitatively on-par with those of the SLD-driven tomogram. The chaotic Kerr comb tomogram visually has a higher amount of speckle noise than the SLD equivalent scan, arising from the semi-coherent nature of the individual comb lines themselves. This speckle noise could potentially be reduced by utilizing higher

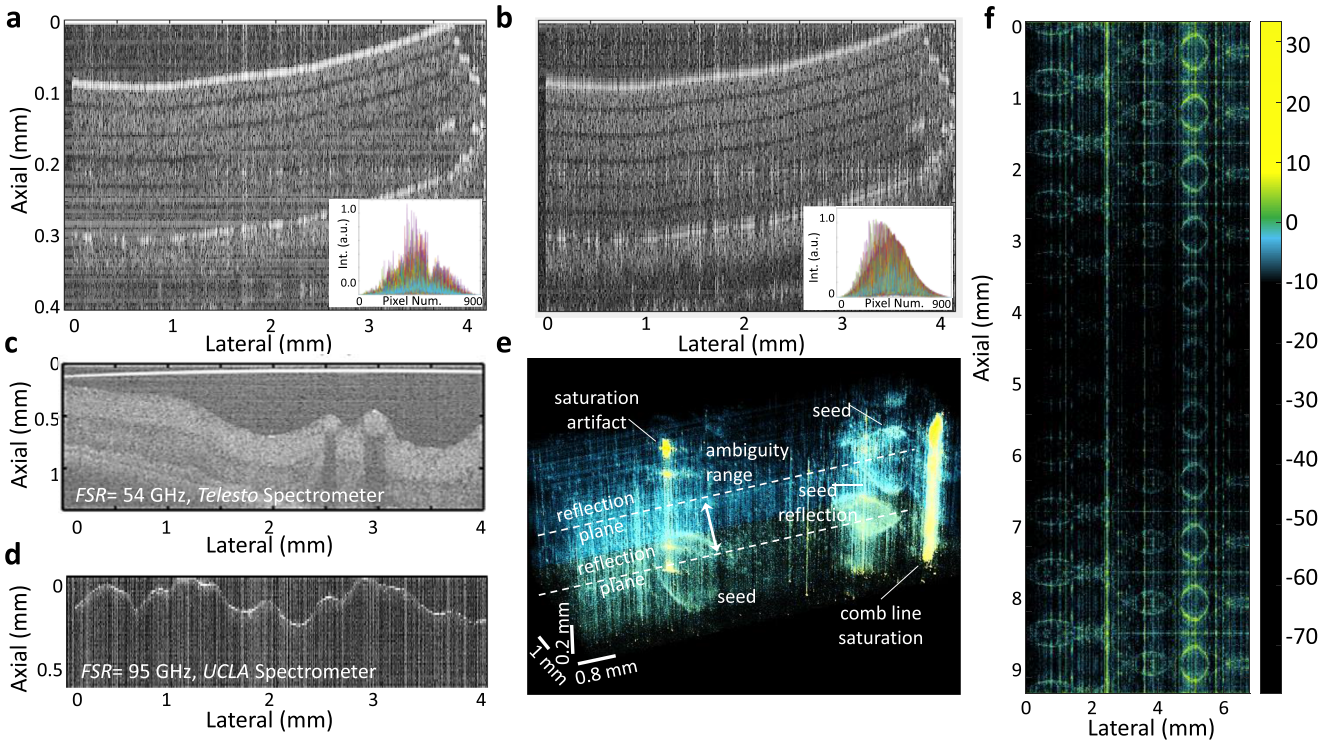

FIG. 4. Laser microcomb OCT tomogram results. (a) 95 GHz frequency-comb lit OCT image of a tape stack based on our UCLA spectrometer. Inset: overlaid interferograms used to generate the OCT image. (b) For comparison, a SLD-lit OCT image of a tape stack based on our UCLA spectrometer. Inset: overlaid interferograms used to generate the OCT image. The tomograms in (a) and (b) are remarkably similar and capture all features of the tape stack, including the staircase-shaped stack edge. (c) Pig retinal OCT image utilizing the 54 GHz frequency microcomb and Telesto spectrometer. (d) 95 GHz microcomb-lit OCT image of orange peel utilizing our UCLA spectrometer. (e) 95 GHz frequency-comb-lit volume scan of the strawberry surface based on our UCLA spectrometer. The image is brightened for clarity. (f) Single B-scan of the strawberry in (e). The color bar shows intensity for (e) and (f) in arbitrary units.

power amplified spontaneous emission from the pump laser combined with the frequency comb, which is an interesting direction for further study.

Figure 4(c) next shows the pig retina OCT B-scan for tissue imaging demonstration. We utilized a 54 GHz laser microcomb and the Telesto spectrometer for this measurement. When using the Telesto II spectrometer, light from the SLD is added to the comb light due to the design of the commercial system. This results in a tomogram that is a combined result of the comb state and the SLD. Tissue structure is visible, and blood vessels can be seen with high contrast, enabling tissue analysis and diagnosis. For an example target with a less regular structure, we also imaged an orange peel with the comb source as illustrated in Fig. 4(d) using the custom UCLA spectrometer. The contours of the peel surface and areas with oils are also clearly visible and are identifiable by the localized bright spots. More visual artifacts exist in this scan in the form of vertical lines, a manifestation of comb line noise in the comb state or individual comb line spectrometer saturation. This effect can be mitigated by utilizing a more stable comb state or increasing the number of averaged tomograms, as noted in Sec. IV below.

Moreover, we perform a volume scan on another sample (a strawberry) to demonstrate the ability to take volumetric data, as shown in Fig. 4(e). We show only a subsection of the overall volume scan for clarity. Surface features such as strawberry seeds are identifiable. We also note the ambiguity range and imaging replica, which are inherent to a discrete-frequency microcomb OCT. Optimizing the distance between the target and the objective to keep the target completely in the frame can mitigate some of the volume scan reflections in the right-most third of the volume, and averaging over multiple volumetric scans could reveal additional structure. Figure 4(f) shows a single B-scan of the strawberry to aid in the visualization of the ambiguity range and repetitive nature of the comb-based tomogram.

For a tomogram to be considered high quality, a strong distinction between highly reflecting structural pixels vs weakly reflecting or transparent pixels should be apparent. We utilize the recently developed maximum tissue contrast (mTCI) and quality index (QI) metrics over the region occupied by the target.[56,66] mTCI is a quantitative method of tomogram assessment based on the ratio of background and foreground pixels in an image, interpreted from a histogram of pixel intensities.[56] The quantity is defined as

$$mTCI = \frac{N_3 - N_1}{N_2 - N_1}, \tag{7}$$

where N_1 is the mainlobe peak of the background pixels, N_2 is the intersection of the background and foreground pixel lobes, and N_3 is the saturation point.[56] A larger mTCI score generally depicts a better contrast in the obtained images. From the tomograms of Figs. 3(a) and 3(b), we find a mTCI of 5.2 for the frequency comb tomogram and 2.6 for the SLD tomogram.

In conjunction, we calculate the quality index, QI, of both images. This is obtained by taking the intensity ratio (akin to a signal-to-noise ratio),

$$IR = \frac{h(N_{sat}) - h(N_{low})}{h(N_{low})}, \tag{8}$$

and multiplying by the tissue signal ratio (TSR),

$$TSR = \frac{\sum_{N_{mid}}^{N_{sat}} h(i)}{\sum_{N_{noise}}^{N_{mid}} h(j)} \tag{9}$$

so that $QI = IR \times TSR$, where N_{sat}, N_{noise}, N_{low}, and N_{mid} are the points where the intensity values represent the 99th percentile, 75th percentile, 1st percentile, and mean of noise and saturation, respectively. Here, $h(n)$ is the intensity histogram corresponding to the tomogram in question.[57] The noise threshold is chosen to discriminate against most of the pixels that may be interpreted as noise and only include pixels that most likely represent the relevant signal. We find a QI of 26.2 for the frequency comb tomogram [Fig. 3(a)] and 4.5 for the SLD tomogram [Fig. 3(b)]. Details regarding the algorithms and calculations of both mTCI and QI, as well as their relative significance as a performance score, are noted in the supplementary material 1.

V. CONCLUSION

In this work, we demonstrated a laser frequency microcomb-based 1-μm OCT imaging subsystem. We show that the resolution achieved is comparable to or exceeds that of the equivalent commercially available system. The broader optical spectrum of the chaotic microcomb provides higher axial resolution, and through tomogram averaging, the influence of random comb line intensity fluctuations is reduced, thus enabling a less distorted and clearer tomogram. With the comb state properly chosen and appropriate tuning of the OCT system, our scans show tomograms with little distortion or additional noise from the frequency microcomb, with images similar to the commercially available system. In fact, the previously developed tomogram quantification metrics mTCI and QI indicate equivalent or superior tomograms when compared to conventional SLD-based counterparts. However, mTCI and QI are not perfect metrics since both make the key assumption that all brightly reflecting pixels are indicative of the imaged structure. This means that tomograms with a non-negligible amount of high-amplitude noise, such as that arising from spectrometer saturation by an individual comb line, could result in an inflated mTCI and QI score (see the supplementary material 1). With these considerations in mind, these two metrics can be applied appropriately when tomograms do not have sizable noise of this nature.

We further demonstrate the axial resolution matching or surpassing that of the original Telesto II OCT instrument, which has an instrument-specified 20 μm axial resolution. We surpassed the original instrument specification with our frequency microcomb OCT in combination with a necessary custom-built spectrometer with a larger bandwidth for an achieved axial resolution of 5.65 ± 1.7 μm. Current axial resolution measurements match the theoretical estimate of 6.2 μm and could be reduced further by increasing the comb bandwidth. Table III outlines several comparable works to this paper, with this work in bold. Our source matches or is superior to many of these sources, only surpassed by those that are not chip-scale.

This work also highlights an advantage of the frequency comb OCT over SLD-based imaging in that multiple microresonators

TABLE III. Selected works for comparison of OCT source performance. The bold row is from this work.

References	Source type	Chip-scale	Center wavelength (nm)	Axial resolution in air (μm)
Telesto II	Superluminescent diode	Yes	1064	20
67	Superluminescent diode	Yes	840	15
68	Supercontinuum	No	775	2.0
60	Chaotic Kerr comb	Yes	1311.66	18
14	Supercontinuum	Yes	1300	7.28
15	Frequency comb	No	840	5
62	Soliton frequency comb	Yes	1300	6
This work	**Chaotic Kerr comb**	**Yes**	**1064**	**5.65**

providing various comb characteristics can be nanofabricated in-parallel on a semiconductor chip with high repeatability. This provides control over the trade-off between axial resolution and imaging depth by switching between different microcombs on the same chip for imaging. In addition, low-power, turnkey operation of frequency combs has been developed, simplifying the driving electronics needed for practical implementation into OCT systems.[32] With self-coupling systems to automate the coupling process to the specific resonator, these two parameters could be configured on-the-fly by selecting different resonators for more useful and clearer tomograms in ophthalmic applications at different depths. However, as previously mentioned, due to the chaotic nature of the comb state, multiple tomograms must be averaged together to achieve decent imaging results. This slows down the effective tomogram acquisition rate by the number of tomograms being averaged, which for this work slows our speed to only 10% of the actual B-scan imaging rate. To address this, future research is directed toward operating frequency combs in the soliton regime, eliminating the need to average multiple tomograms to achieve decent imaging results. The axial resolution and imaging depth trade-off is another limitation the frequency comb-based implementation suffers from, and several techniques have been developed that are able to reconstruct the undersampled data.[69–72] In addition, a novel method to address the trade-off between imaging depth and resolution is being developed to operate in conjunction with the soliton state. The observed axial resolution, in conjunction with a CMOS-compatible and highly manufacturable microcomb structure, demonstrates the potential of a chip-scale platform for unique diagnostic tomography.

SUPPLEMENTARY MATERIAL

The supplementary material contains in-depth information on the definitions and use of mTCI and QI. It also contains further explanations of the axial resolution analysis and the custom-built spectrometer.

ACKNOWLEDGMENTS

The authors acknowledge the discussions with Dr. Abhinav Kumar Vinod and Dr. Hao Liu for their contributions toward microresonator design. This work received the funding support from the UCLA Innovation Fund, the Alcon Research Institute, a Departmental Grant from Research to Prevent Blindness to UCLA's Department of Opthalmology, and an unrestricted grant from Heidelberg Engineering.

AUTHOR DECLARATIONS

Conflict of Interest

The authors have no conflicts to disclose.

Author Contributions

T.M., J.F.M. and J.Y. contributed equally to this work.

J.Y. and J.F.M. developed the idea and constructed the measurement setup. T.M., J.F.M., J.Y., and W.W. conducted the measurements. T.M., J.F.M., and J.Y. performed data analysis. Y.L., M.G., M.R., J.P.H., K.N.-M., and C.W.W. supported and discussed the studies. T.M. prepared the manuscript. C.W.W. supervised the project. All authors contributed to the discussion and revision of the manuscript.

T. Melton: Data curation (equal); Formal analysis (equal); Methodology (equal); Project administration (equal); Software (equal); Supervision (equal); Validation (equal); Visualization (equal); Writing – original draft (equal); Writing – review & editing (equal). **J. F. McMillan**: Conceptualization (equal); Data curation (equal); Formal analysis (equal); Investigation (equal); Methodology (equal); Project administration (equal); Resources (equal); Software (equal); Supervision (equal); Validation (equal). **J. Yang**: Conceptualization (equal); Formal analysis (equal); Investigation (equal); Methodology (equal); Project administration (equal); Supervision (equal). **W. Wang**: Formal analysis (equal); Investigation (equal). **Y. Lai**: Investigation (equal); Resources (equal). **M. Gerber**: Formal analysis (equal); Methodology (equal); Project administration (equal). **M. Rodriguez**: Investigation (equal). **J. P. Hubschman**: Investigation (equal); Project administration (equal); Supervision (equal). **K. Nouri-Mahdavi**: Conceptualization (equal); Formal analysis (equal); Investigation (equal); Project administration (equal); Resources (equal); Writing – review & editing (equal). **C. W. Wong**:

Conceptualization (equal); Formal analysis (equal); Funding acquisition (equal); Investigation (equal); Project administration (equal); Resources (equal); Supervision (equal); Writing – review & editing (equal).

DATA AVAILABILITY

The data that support the findings of this study are available from the corresponding authors upon reasonable request.

REFERENCES

[1] D. Huang, E. Swanson, C. Lin, J. Schuman, W. Stinson, W. Chang, M. Hee, T. Flotte, K. Gregory, C. A. Puliafito, and J. Fujimoto, "Optical coherence tomography," Science **254**, 1178–1181 (1991).

[2] W. Drexler and J. Fujimoto, *Optical Coherence Tomography: Technology and Applications* (Springer, Berlin, Germany, 2008).

[3] A. F. Fercher, W. Drexler, C. K. Hitzenberger, and T. Lasser, "Optical coherence tomography—Principles and applications," Rep. Prog. Phys. **66**, 239–303 (2003).

[4] J. F. Bille, *High Resolution Imaging in Microscopy and Ophthalmology: New Frontiers in Biomedical Optics* (Springer International Publishing, Cham, 2019).

[5] S. H. Kassani, M. Villiger, N. Uribe-Patarroyo, C. Jun, R. Khazaeinezhad, N. Lippok, and B. E. Bouma, "Extended bandwidth wavelength swept laser source for high resolution optical frequency domain imaging," Opt. Express **25**, 8255–8266 (2017).

[6] B. J. Vakoc, R. M. Lanning, J. A. Tyrrell, T. P. Padera, L. A. Bartlett, T. Stylianopoulos, L. L. Munn, G. J. Tearney, D. Fukumura, R. K. Jain, and B. E. Bouma, "Three-dimensional microscopy of the tumor microenvironment *in vivo* using optical frequency domain imaging," Nat. Med. **15**, 1219–1223 (2009).

[7] T. Bolmont, A. Bouwens, C. Pache, M. Dimitrov, C. Berclaz, M. Villiger, B. M. Wegenast-Braun, T. Lasser, and P. C. Fraering, "Label-free imaging of cerebral β-amyloidosis with extended-focus optical coherence microscopy," J. Neurosci. **32**, 14548–14556 (2012).

[8] V. J. Srinivasan, H. Radhakrishnan, J. Y. Jiang, S. Barry, and A. E. Cable, "Optical coherence microscopy for deep tissue imaging of the cerebral cortex with intrinsic contrast," Opt. Express **20**, 2220–2239 (2012).

[9] R. Leitgeb, C. K. Hitzenberger, and A. F. Fercher, "Performance of Fourier domain vs time domain optical coherence tomography," Opt. Express **11**, 889–894 (2003).

[10] J. F. de Boer, B. Cense, B. H. Park, M. C. Pierce, G. J. Tearney, and B. E. Bouma, "Improved signal-to-noise ratio in spectral-domain compared with time-domain optical coherence tomography," Opt. Lett. **28**, 2067–2069 (2003).

[11] M. A. Choma, M. V. Sarunic, C. Yang, and J. A. Izatt, "Sensitivity advantage of swept source and Fourier domain optical coherence tomography," Opt. Express **11**, 2183–2189 (2003).

[12] W. J. Choi and R. K. Wang, "Swept-source optical coherence tomography powered by a 1.3-μm vertical cavity surface emitting laser enables 2.3-mm-deep brain imaging in mice *in vivo*," J. Biomed. Opt. **20**, 106004 (2015).

[13] W. Drexler, "Ultrahigh-resolution optical coherence tomography," J. Biomed. Opt. **9**, 47–74 (2004).

[14] X. Ji, D. Mojahed, Y. Okawachi, A. L. Gaeta, C. P. Hendon, and M. Lipson, "Millimeter-scale chip-based supercontinuum generation for optical coherence tomography," Sci. Adv. **7**, eabg8869 (2021).

[15] T. Bajraszewski, M. Wojtkowski, M. Szkulmowski, A. Szkulmowska, R. Huber, and A. Kowalczyk, "Improved spectral optical coherence tomography using optical frequency comb," Opt. Express **16**, 4163–4176 (2008).

[16] T.-H. Tsai, C. Zhou, D. C. Adler, and J. G. Fujimoto, "Frequency comb swept lasers," Opt. Express **17**, 21257–21270 (2009).

[17] E. J. Jung, J. S. Park, M. Y. Jeong, C. S. Kim, T. J. Eom, B. A. Yu, S. Gee, J. Lee, and M. K. Kim, "Spectrally-sampled OCT for sensitivity improvement from limited optical power," Opt. Express **16**, 17457–17467 (2008).

[18] M. Siddiqui, A. S. Nam, S. Tozburun, N. Lippok, C. Blatter, and B. J. Vakoc, "High-speed optical coherence tomography by circular interferometric ranging," Nat. Photonics **12**, 111–116 (2018).

[19] P. Del'Haye, A. Schliesser, O. Arcizet, T. Wilken, R. Holzwarth, and T. J. Kippenberg, "Optical frequency comb generation from a monolithic microresonator," Nature **450**, 1214–1217 (2007).

[20] T. J. Kippenberg, R. Holzwarth, and S. A. Diddams, "Microresonator-based optical frequency combs," Science **332**, 555–559 (2011).

[21] T. J. Kippenberg, A. L. Gaeta, M. Lipson, and M. L. Gorodetsky, "Dissipative Kerr solitons in optical microresonators," Science **361**, eaan8083 (2018).

[22] S. W. Huang, H. Zhou, J. Yang, J. F. McMillan, A. Matsko, M. Yu, D. L. Kwong, L. Maleki, and C. W. Wong, "Mode-locked ultrashort pulse generation from on-chip normal dispersion microresonators," Phys. Rev. Lett. **114**, 053901 (2015).

[23] M. L. Gorodetsky, "Dissipative Kerr combs in microresonators: From chaos to solitons," in 2016 International Conference Laser Optics, 2016.

[24] Z. Sun, Y. Li, B. Bai, Z. Zhu, and H. B. Sun, "Silicon nitride-based Kerr frequency combs and applications in metrology," Adv. Photonics **4**, 064001 (2022).

[25] H. Zhou, S. W. Huang, Y. Dong, M. Liao, K. Qiu, and C. W. Wong, "Stability and intrinsic fluctuations of dissipative cavity solitons in Kerr frequency microcombs," IEEE Photonics J. **7**, 3200113 (2015).

[26] S. W. Huang, J. Yang, J. Lim, H. Zhou, M. Yu, D. L. Kwong, and C. W. Wong, "A low-phase-noise 18 GHz Kerr frequency microcomb phase-locked over 65 THz," Sci. Rep. **5**, 13355 (2015).

[27] Y. Okawachi, K. Saha, J. S. Levy, Y. H. Wen, M. Lipson, and A. L. Gaeta, "Octave-spanning frequency comb generation in a silicon nitride chip," Opt. Lett. **36**, 3398–3400 (2011).

[28] S. Coen, H. G. Randle, T. Sylvestre, and M. Erkintalo, "Modeling of octave-spanning Kerr frequency combs using a generalized mean-field Lugiato–Lefever model," Opt. Lett. **38**, 37–39 (2013).

[29] M. H. P. Pfeiffer, C. Herkommer, J. Liu, H. Guo, M. Karpov, E. Lucas, M. Zervas, and T. J. Kippenberg, "Octave-spanning dissipative Kerr soliton frequency combs in Si_3N_4 microresonators," Optica **4**, 684–691 (2017).

[30] Q. Li, T. C. Briles, D. A. Westly, T. E. Drake, J. R. Stone, B. R. Ilic, S. A. Diddams, S. B. Papp, and K. Srinivasan, "Stably accessing octave-spanning microresonator frequency combs in the soliton regime," Optica **4**, 193–203 (2017).

[31] J. Liu, A. S. Raja, M. Karpov, B. Ghadiani, M. H. P. Pfeiffer, B. Du, N. J. Engelsen, H. Guo, M. Zervas, and T. J. Kippenberg, "Ultralow-power chip-based soliton microcombs for photonic integration," Optica **5**, 1347–1353 (2018).

[32] B. Stern, X. Ji, Y. Okawachi, A. L. Gaeta, and M. Lipson, "Battery-operated integrated frequency comb generator," Nature **562**, 401–405 (2018).

[33] T. J. Kippenberg, S. M. Spillane, and K. J. Vahala, "Kerr nonlinearity optical parametric oscillation in an ultrahigh-*Q* toroid microcavity," Phys. Rev. Lett. **93**, 083904 (2004).

[34] M.-G. Suh, Q.-F. Yang, K. Y. Yang, X. Yi, and K. J. Vahala, "Microresonator soliton dual-comb spectroscopy," Science **354**, 600–603 (2016).

[35] J. Lim, S. W. Huang, A. K. Vinod, P. Mortazavian, M. Yu, D. L. Kwong, A. A. Savchenkov, A. B. Matsko, L. Maleki, and C. W. Wong, "Stabilized chip-scale Kerr frequency comb via a high-*Q* reference photonic microresonator," Opt. Lett. **41**, 3706 (2016).

[36] S. W. Huang, A. K. Vinod, J. Yang, M. Yu, D. L. Kwong, and C. W. Wong, "Quasi-phase-matched multispectral Kerr frequency comb," Opt. Lett. **42**, 2110 (2017).

[37] S. W. Huang, J. Yang, S. H. Yang, M. Yu, D. L. Kwong, T. Zelevinsky, M. Jarrahi, and C. W. Wong, "Globally stable microresonator Turing pattern formation for coherent high-power THz radiation on-chip," Phys. Rev. X **7**, 041002 (2017).

[38] H. Zhou, Y. Geng, W. Cui, S. W. Huang, Q. Zhou, K. Qiu, and C. Wei Wong, "Soliton bursts and deterministic dissipative Kerr soliton generation in auxiliary-assisted microcavities," Light: Sci. Appl. **8**, 50 (2019).

[39] Y. Li, S. W. Huang, B. Li, H. Liu, J. Yang, A. K. Vinod, K. Wang, M. Yu, D. L. Kwong, H. T. Wang, K. K. Y. Wong, and C. W. Wong, "Real-time transition dynamics and stability of chip-scale dispersion-managed frequency microcombs," Light: Sci. Appl. **9**, 52 (2020).

[40] J. Yang, S. W. Huang, Z. Xie, M. Yu, D. L. Kwong, and C. W. Wong, "Coherent satellites in multispectral regenerative frequency microcombs," Commun. Phys. **3**, 27 (2020).

[41] A. K. Vinod, S. W. Huang, J. Yang, M. Yu, D. L. Kwong, and C. W. Wong, "Frequency microcomb stabilization via dual-microwave control," Commun. Phys. **4**, 81 (2021).

[42]S. W. Huang, J. Yang, M. Yu, B. H. Mcguyer, D. L. Kwong, T. Zelevinsky, and C. W. Wong, "A broadband chip-scale optical frequency synthesizer at 2.7×10^{-16} relative uncertainty," Sci. Adv. **2**, 4 (2016).
[43]C. Bao, Y. Xuan, C. Wang, J. A. Jaramillo-Villegas, D. E. Leaird, M. Q., and A. M. Weiner, "Soliton repetition rate in a silicon-nitride microresonator," Optics Letters **42**, 759–762 (2017).
[44]X. Xue, Y. Xuan, Y. Liu, P. H. Wang, S. Chen, J. Wang, D. E. Leaird, M. Qi, and A. M. Weiner, "Mode-locked dark pulse Kerr combs in normal-dispersion microresonators," Nat. Photonics **9**, 594–600 (2015).
[45]B. Yao, S. W. Huang, Y. Liu, A. K. Vinod, C. Choi, M. Hoff, Y. Li, M. Yu, Z. Feng, D. L. Kwong, Y. Huang, Y. Rao, X. Duan, and C. W. Wong, "Gate-tunable frequency combs in graphene–nitride microresonators," Nature **558**, 410–414 (2018).
[46]J. M. C. Boggio, D. Bodenmüller, S. Ahmed, S. Wabnitz, D. Modotto, and T. Hansson, "Efficient Kerr soliton comb generation in micro-resonator with interferometric back-coupling," Nat. Commun. **13**, 1292 (2022).
[47]S. Kar, M. Saha, S. K. Bag, R. K. Sinha, S. Sharma, S. Singhal, and S. K. Varshney, "Cold-resonance-mediated self-stabilization of Kerr frequency combs in a Si_3N_4 microring resonator," Phys. Rev. A **106**, 013517 (2022).
[48]H. Jung, C. Xiong, K. Y. Fong, X. Zhang, and H. X. Tang, "Optical frequency comb generation from aluminum nitride microring resonator," Opt. Lett. **38**, 2810 (2013).
[49]W. Wang, P.-K. Lu, A. K. Vinod, D. Turan, J. F. McMillan, H. Liu, M. Yu, D.-L. Kwong, M. Jarrahi, and C. W. Wong, "Coherent terahertz radiation with 2.8-octave tunability through chip-scale photomixed microresonator optical parametric oscillation," Nat. Commun. **13**, 5123 (2022).
[50]H. Liu, W. Wang, J. Yang, M. Yu, D.-L. Kwong, and C. W. Wong, "Observation of deterministic double dissipative-Kerr-soliton generation with avoided mode crossing," Phys. Rev. Res. **5**, 013172 (2023).
[51]A. Aldhafeeri, H.-H. Chin, T. Melton, D. I. Lee, A. Chu, W. Wang, M. Yu, P. G. Q. Lo, D. L. Kwong, and C. W. Wong, "Low phase noise K-band signal generation using polarization diverse single-soliton integrated microcombs," Photonics Res. **12**, 1175 (2024).
[52]C. Y. Wang, T. Herr, P. Del'Haye, A. Schliesser, J. Hofer, R. Holzwarth, T. W. Hänsch, N. Picqué, and T. J. Kippenberg, "Mid-infrared optical frequency combs at 2.5 μm based on crystalline microresonators," Nat. Commun. **4**, 1345 (2013).
[53]I. S. Grudinin, N. Yu, and L. Maleki, "Generation of optical frequency combs with a CaF_2 resonator," Opt. Lett. **34**, 878–880 (2009).
[54]B. J. M. Hausmann, I. Bulu, V. Venkataraman, P. Deotare, and M. Lončar, "Diamond nonlinear photonics," Nat. Photonics **8**, 369–374 (2014).
[55]M. Pu, L. Ottaviano, E. Semenova, and K. Yvind, "Efficient frequency comb generation in AlGaAs-on-insulator," Optica **3**, 823 (2016).
[56]Y. Huang, S. Gangaputra, K. E. Lee, A. R. Narkar, R. Klein, B. E. K. Klein, S. M. Meuer, and R. P. Danis, "Signal quality assessment of retinal optical coherence tomography images," Invest. Ophthalmol. Visual Sci. **53**, 2133–2141 (2012).
[57]D. M. Stein, H. Ishikawa, R. Hariprasad, G. Wollstein, R. J. Noecker, J. G. Fujimoto, and J. S. Schuman, "A new quality assessment parameter for optical coherence tomography," Br. J. Ophthalmol. **90**, 186–190 (2006).
[58]M. Yu, J. K. Jang, Y. Okawachi, A. Griffith, K. Luke, S. A. Miller, X. Ji, M. Lipson, and A. L. Gaeta, "Breather soliton dynamics in microresonators," Nat. Commun. **8**, 14569 (2017).
[59]T. Herr, V. Brasch, J. D. Jost, C. Y. Wang, N. M. Kondratiev, M. L. Gorodetsky, and T. J. Kippenberg, "Temporal solitons in optical microresonators," Nat. Photonics **8**, 145–152 (2014).
[60]X. Ji, X. Yao, A. Klenner, Y. Gan, A. L. Gaeta, C. P. Hendon, and M. Lipson, "Chip-based frequency comb sources for optical coherence tomography," Opt. Express **27**, 19896–19905 (2019).
[61]S. W. Huang, H. Liu, J. Yang, M. Yu, D. L. Kwong, and C. W. Wong, "Smooth and flat phase-locked Kerr frequency comb generation by higher order mode suppression," Sci. Rep. **6**, 26255 (2016).
[62]P. J. Marchand, J. Riemensberger, J. C. Skehan, J. J. Ho, M. H. P. Pfeiffer, J. Liu, C. Hauger, T. Lasser, and T. J. Kippenberg, "Soliton microcomb based spectral domain optical coherence tomography," Nat. Commun. **12**, 427 (2021).
[63]X. Yao, "Ultrahigh resolution spectral domain optical coherence tomography and its functional extension for human myocardium and breast tissue imaging," Ph.D. thesis, Columbia University, 2018.
[64]R. Tripathi, N. Nassif, J. S. Nelson, B. H. Park, and J. F. de Boer, "Spectral shaping for non-Gaussian source spectra in optical coherence tomography," Opt. Lett. **27**, 406–408 (2002).
[65]X. Yao, Y. Gan, C. C. Marboe, and C. P. Hendon, "Myocardial imaging using ultrahigh-resolution spectral domain optical coherence tomography," J. Biomed. Opt. **21**, 61006 (2016).
[66]S. Liu, A. S. Paranjape, B. Elmaanaoui, J. Dewelle, H. G. Rylander III, M. K. Markey, and T. E. Milner, "Quality assessment for spectral domain optical coherence tomography (OCT) images," Proc. SPIE **7171**, 71710X (2009).
[67]N. H. Cho, U. S. Jung, H. I. Kwon, H. S. Jeong, and J. H. Kim, "Development of SD-OCT for imaging the *in vivo* human tympanic membrane," J. Opt. Soc. Korea **15**, 74–77 (2011).
[68]J. Barrick, A. Doblas, M. R. Gardner, P. R. Sears, L. E. Ostrowski, and A. L. Oldenburg, "High-speed and high-sensitivity parallel spectral-domain optical coherence tomography using a supercontinuum light source," Opt. Lett. **41**, 5620–5623 (2016).
[69]X. Li, S. Cao, H. Liu, X. Yao, B. C. Brott, S. H. Litovsky, X. Song, Y. Ling, and Y. Gan, "Multi-scale reconstruction of undersampled spectral-spatial OCT data for coronary imaging using deep learning," IEEE Trans. Biomed. Eng. **69**, 3667–3677 (2022).
[70]Y. Zhang, T. Liu, M. Singh, E. Çetintaş, Y. Luo, Y. Rivenson, K. V. Larin, and A. Ozcan, "Neural network-based image reconstruction in swept-source optical coherence tomography using undersampled spectral data," Light: Sci. Appl. **10**, 155 (2021).
[71]Z. Gong, Y. Shi, and R. K. Wang, "De-aliased depth-range-extended optical coherence tomography based on dual under-sampling," Opt. Lett. **47**, 2642–2645 (2022).
[72]Z. Wang, Z. Yuan, H. Wang, and Y. Pan, "Increasing the imaging depth of spectral-domain OCT by using interpixel shift technique," Opt. Express **14**, 7014–7023 (2006).